BiO_mF_n/BiO_xI_y/GO NANOCOMPOSITES: SYNTHESIS, CHARACTERIZATION, AND PHOTCATALYTIC ACTIVITY

Jing-Ya Fu[1], Yong-Ming Dai[1], Li-Wen Chen[1], Chiing-Chang Chen[2]*

[1] Department of Science Education and Application, National Taichung University of Education, Taichung 40306, Taiwan, ra23372001@yahoo.com.tw; forest1105@gmail.com; liwenchen@mail.ntcu.edu.tw

[2] Department of Science Education and Application, National Taichung University of Education, Taichung 40306, Taiwan; ccchen@mail.ntcu.edu.tw; http://home.ntcu.edu.tw/SCIENCE/people/bio.php?PID=8

Keywords: Bismuth oxyfluoride, Bismuth oxyiodide, Graphene oxide, Composites, Photocatalytic

ABSTRACT

This is the first report that a series of bismuth oxyfluoride/bismuth oxyiodide/graphene oxide (BiO_mF_n/BiO_xI_y/GO) nanocomposites with different GO contents are synthesized through a simple hydrothermal method and characterized using XRD, TEM, SEM-EDS, FT-IR, XPS, BET, and DRS. The BiO_mF_n/BiO_xI_y/GO composites exhibit excellent photocatalytic activities in the degradation of crystal violet (CV) and salicylic acid (SA) under visible light irradiation. The order of rate constants appears $Bi_{50}O_{59}F_{32}$/BiOI/GO > BiOF/BiOI/GO > BiOI > $Bi_{50}O_{59}F_{32}$/BiOI/Bi_5O_7I/GO > BiOF > GO. The photocatalytic activity of $Bi_{50}O_{59}F_{32}$/BiOI/GO composites reaches a maximum rate constant of 0.2539 h^{-1}, which is 1.1 times higher than that of $Bi_{50}O_{59}F_{32}$/BiOI, 1.3 and 110 times higher than that of BiOI and $Bi_{50}O_{59}F_{32}$.

1 INTRODUCTION

Semiconductor photo-catalysis driven by visible light has sparked great research interest because it provides a valuable method for solving environmental pollution and energy supply problems. An environmentally potent and cheap photo-catalyst is an important component for practical applications of photo-catalysis [1]. The study of visible-light-driven photo-catalysts has attracted considerable attention as an alternative to the elimination of toxic materials from wastewater. The photo-catalytic degradation of CV dyes was researched using several systems to produce active species including BiO_xCl_y/BiO_mI_n [2], BiOBr/BiOI [3], $BaTiO_3$ [4], BiOI [5], Bi_2WO_6 [6], $PbBiO_2Br$/BiOBr [7], BiOI/GO [8], Bi_2SiO_5/g-C_3N_4 [9], and $SrFeO_{3-x}$/g-C_3N_4 [10]. A simple and effective strategy for improving the photo-catalytic activity of a photo-catalyst is the incorporation of a hetero-structure because it has great potential for tuning the desired electronic properties of photo-catalysts and efficiently separating photo-induced electron–hole pairs.

Bismuth oxyhalide compounds (BiOX, X = F, Cl, Br, I) have been investigated widely because of their chemical stability, unique layer structure and excellent photocatalytic performance under UV or visible-light illumination. BiOX has received increasing interests because of its suitable energy gaps, stability, and relatively superior photo-catalytic activities [11,12]. Among them, BiOF is a direct band gap photocatalyst with a band gap of ~3.5 eV which makes it sensitive to UV region. The atomic arrangements in BiOF consists of $[Bi_2O_2]^{2+}$ slabs which are sandwiched by two fluorine atoms $[F_2]^{2-}$ to form $[Bi_2O_2F_2]$ layers. However, because the valence band for bismuth oxyiodides contains mostly I_{5p} and O_{2p} orbitals, whereas the conduction band is based on the Bi_{6p} orbital [13], iodine-poor BiO_mI_n could be demonstrated to have band-gap energy lower than it of Bi_2O_3 but higher than it of BiOI [14]; hence, these materials might be used as visible-light responsive photocatalysts. In particular, the structure and composition of BiO_mI_n strongly influence their optical, electronic, oxidizing abilities, and other physicochemical properties, offering an opportunity to obtain novel photocatalysts for effective degradation of environmental and toxic pollutants. Following Keller and Kramer [15] who have first reported the practically unlimited solubility of the BiOX/BiOY (X, Y = Cl, Br, I) systems,

several articles were published disclosing the successful synthesis and the unique photocatalytic properties of similar oxyhalide materials. However, the synthesis methods, characterization, and evaluated properties of a series of BiOX/BiOY have remained rare until recently.

Graphene (GR) and its derivatives are excellent electron mediators due to their unique two-dimensional structures and superior conductivity, and have attracted numerous attentions recently [16]. Therefore, it can be used as an ideal support material with improved interfacial contact and enhanced adsorption activity. GR has a powerful but flexible structure with high carrier mobility. Thus, a GR-based hybrid photocatalyst will show excellent photocatalytic efficiency, such as, BiOI/GR [17] and BiOBr/GR [18]. Two specific branches of GR research dealt with graphene oxide (GO) and reduced graphene oxide (rGO). This could be considered as a precursor of semiconductor/GO (or rGO) synthesis by either chemical or thermal processes. A previous study showed that the incorporation of GO with a metal oxide could enhance the photocatalytic activity [19-21].

According to our literature search, a series of BiO_mF_n/BiO_xI_y/GO-assisted photocatalytic degradation of CV dyes under visible light irradiation has never been reported. This study synthesizes a series of BiO_mF_n/BiO_xI_y/GO nanocomposites with different GO contents, synthesizes through a simple hydrothermal method, and compares their photocatalytic activities in degrading CV in aqueous solutions under visible light irradiation. Possible photo-degradation mechanisms are proposed and discussed in this research. The study is useful in synthesizing BiO_mF_n/BiO_xI_y/GO and degrading dye for the future applications of environmental pollution and control.

2 EXPERIMENTAL DETAILS

2.1 Synthesis of BiO_mCl_n/BiO_xI_y/GO

GO was synthesized by stirring 1 g powdered flake graphite and 0.5 g $NaNO_3$ into 23 mL H_2SO_4 at 0 °C ice bath. While maintaining vigorous agitation, 3 g $KMnO_4$ was added to the suspension. The ice bath was then removed, and the temperature of the suspension was brought to 35 °C and maintained at that temperature overnight. Then, 3 g $KMnO_4$ was added to the suspension, which was allowed to stand for 3h. After 3h, 46 mL H_2O was slowly stirred into the paste, causing violent effervescence and the temperature increasing to 95 °C. The diluted suspension, now brown in color, was maintained at this temperature for 15 min. The suspension was then further diluted to approximately 140 mL with warm water and treated with 30% (w) H_2O_2 to reduce the residual MnO_4^- and MnO_2 to bleach soluble $Mn(SO_4)_2$. Upon the treatment with peroxide, the suspension turned bright yellow. The suspension was filtered, and a yellow-brown filter cake was obtained. After washing the cake three times with a total of 140 mL warm water, the GO residue was dispersed in 100 mL of 10% HCl. Dry GO was obtained through centrifugation followed by drying in the oven at 60 °C overnight [8,22].

Five mmol $Bi(NO_3)_3•5H_2O$ was first mixed in a 50-mL flask and then added 5 mL 4 M ethylene glycerol and GO powder. With continuous stir, 2 M NaOH was added dropwise to adjust the pH value; when a precipitate was formed, 2 mL KI and KF were also added dropwise. The solution was then stirred vigorously for 30 min and transferred into a 30 mL Teflon-lined autoclave, which was heated to 100–250 °C for 12 h and then naturally cooled to room temperature. The resulting solid precipitate was collected by filtration, washed with deionized water and methanol to remove any possible ionic species in the solid precipitate, and then dried at 60 °C overnight. Depending on the molar ratio of $Bi(NO_3)_3•5H_2O$ to KI or KF, pH value, temperature, and time, different BiO_mF_n/BiO_xI_y/GO samples could be synthesized.

2.2 Photocatalytic and active species experiments

CV irradiation experiments were conducted on a stirred aqueous solution contained in a 100-mL flask; the aqueous suspension of CV (100 mL, 10 ppm) and a catalyst powder were placed in a Pyrex flask. The pH of the suspension was adjusted by adding either NaOH or HNO_3 solution. Dark experiments were performed to examine the adsorption or desorption equilibrium. Ten mg photocatalyst was mixed with 100 mL aqueous CV solution with a known initial concentration in a 100-mL flask, and the mixture was shaken in an orbital shaker (100 rpm) at a constant temperature.

The mixture was centrifuged at 3000 rpm in a centrifugation machine after batch sorption experiments so that the absorbance of CV could be determined at 580 nm through HPLC photo-diode array electrospray ionization mass spectrometry (HPLC-PDA-ESI-MS). The concentrations of the solutions were determined using a linear regression equation. Prior to irradiation, the suspension was magnetically stirred in the dark for approximately 30 min to establish an adsorption or desorption equilibrium between the CV and the catalyst surface. Irradiation was conducted using 150 W Xe arc lamps with the light intensity fixed at 31.1 W/m^2, and the reaction vessel was placed 30 cm from the light source. At given irradiation time intervals, a 5-mL aliquot was collected and centrifuged to remove the catalyst. The supernatant was measured using HPLC-PDA-ESI-MS.

A series of quenchers were introduced to scavenge the relevant active species to evaluate the effect of the active species during the photocatalytic reaction. Superoxide radical, hydroxyl radical, hole, and singlet oxygen ($^1O_2$) were studied by adding 1.0 mM benzoquinone (BQ, a quencher of superoxide radical), 1.0 mM isopropanol (IPA, a quencher of hydroxyl radical), 1.0 mM ammonium oxalate (AO, a quencher of hole), and 1.0 mM sodium azide (SA, a quencher of singlet oxygen). The method was similar to the previously reported photocatalytic activity test [2,3].

3 RESULTS AND DISCUSSION

3.1 Characterization of BiO_mF_n/BiO_xI_y/GO composites

Figure 1 shows the XRD patterns of the as-prepared samples; the patterns clearly show the existence of different BiO_mF_n/BiO_xI_y phase composites with GO. All the as-prepared samples contain BiOF phase (JCPDS 73-1595), $Bi_{50}O_{59}F_{32}$ phase (JCPDS 24-0145), $Bi_{26}O_{38}F_2$ phase (JCPDS 41-0617), BiOI phase (JCPDS 10-0445), $Bi_7O_9I_3$ phase [23], Bi_5O_7I phase (JCPDS 40-0548), and GO [24]. At GO = 0 g, the XRD patterns are identical to those reported for $Bi_{50}O_{59}F_{32}$/BiOI/GO ternary phases; at GO = 0.05-0.05g, the XRD patterns are identical to those reported for $Bi_{26}O_{38}F_{22}$/BiOI/GO ternary phases; at GO = 0.1g, the XRD patterns are identical to those reported for BiOF/BiOI/GO ternary phases. **Table 1** summarizes the results of the XRD measurement at different pH value and GO amount.

In **Figure 2**, the HRTEM image shows that four sets of different lattice images are found with a d-spacing of 0.3140 and 0.2841 nm, corresponding to the (103) plane of $Bi_{50}O_{59}F_{32}$ and the (110) plane of BiOI which is in satisfactory agreement with the XRD results (**Figure 1**). The results suggest that the series of BiO_mF_n/BiO_xI_y phases are produced in the composites, which are favorable for the separation of photoinduced carriers, yielding high photocatalytic activities.

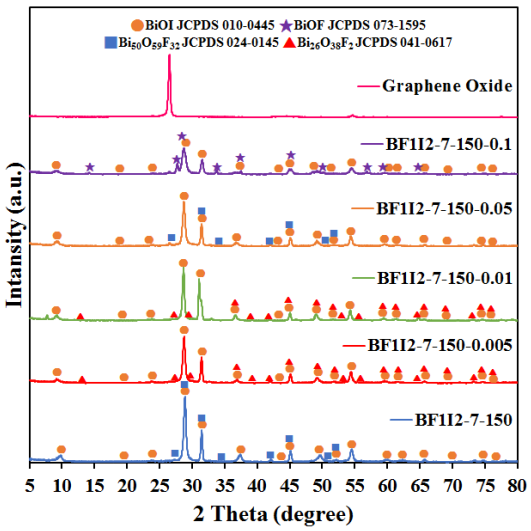

Figure 1. XRD patterns of as-prepared BiO_mF_n/BiO_xI_y/GO samples at different amount of GO. (Hydrothermal conditions: molar ratio KF/KI

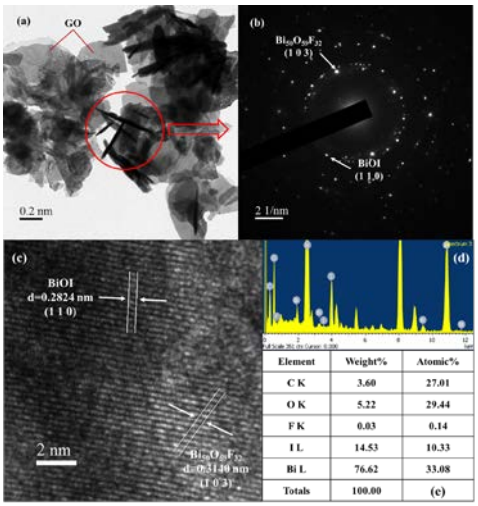

Figure 2. (a) FE-TEM image, (b) SAD, (c) HR-TEM image, (d) and (e) EDS of $Bi_{50}O_{59}F_{32}$/BiOI/GO (BF1I2-7-150-0.05)

= 1/2, GO = 0-0.1 g, pH = 7, Temp = 150 ºC, Time = 12h)

sample by the hydrothermal autoclave method.

Temperature = 150 ºC	GO (g)				
pH value	0	0.005	0.01	0.05	0.1
1	□★	□★	□★	□★	□★
4	□★	□★	□★	□★	□★
7	□▒	□▲	□▲	□▲	□★
10	□◆▲	□◆▲	□◆▲	□◆▲	□◆▲
13	◆▲	□◆▲	□◆▲	□◆▲	□◆▲

Table 1. Crystalline phase changes of as-prepared samples under different hydrothermal conditions. (Hydrothermal conditions: molar ratio KF/KI = 1/2, GO = 0-0.1g, temp = 150°C, pH = 1-13, time = 12 h). □**BiOI** ◆**Bi_5O_7I** ★**BiOF** ▒**$Bi_{50}O_{59}F_{32}$** ▲**$Bi_{26}O_{38}F_2$**

The results illustrate that, at different pH values, a series of changes occur in the products. The results explain that a series of changes in the compounds occur at different hydrothermal conditions, expressed as BiOF →$Bi_{50}O_{59}F_{32}$ → $Bi_{26}O_{38}F_2$ → α-Bi_2O_3 and BiOI → $Bi_4O_5I_2$ → $Bi_7O_9I_3$ → Bi_3O_4I → Bi_5O_7I → α-Bi_2O_3. By controlling the pH of the hydrothermal reaction, different compositions of bismuth oxyhalides are obtained.

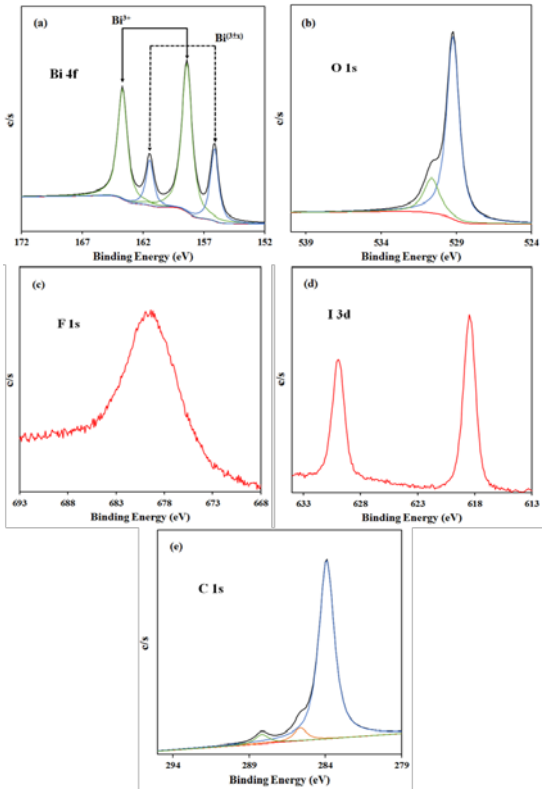

Figure 3. High resolution XPS spectra of as-prepared $Bi_{50}O_{59}F_{32}$/BiOI/GO (BF1I2-7-150-0.05) sample. (a) Bi 4f; (b) O 1s; (c) F 1s; (d) I 3d; (e) C 1s.

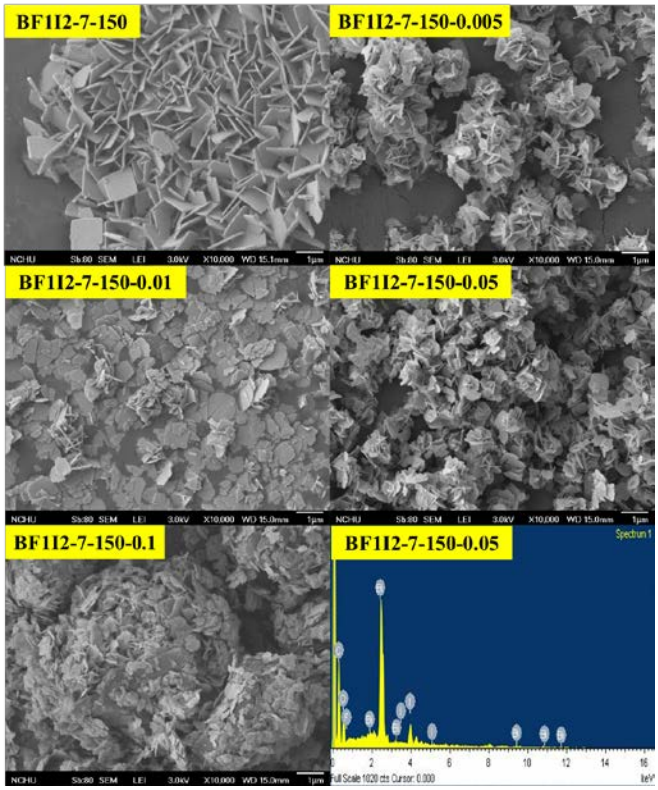

Figure 4. SEM images of as-prepared samples by the hydrothermal method at different amount of GO. (Hydrothermal conditions: molar ratio KF/KI = 1/2, temp = 150°C, pH = 7, time = 12 h)

XPS is used for measuring the purity of the prepared samples. The spectra presented in **Figure 3** are Bi 4f, O 1s, F 1s, and I 3d for the $Bi_{50}O_{59}F_{32}$/BiOI/GO samples. The transition peaks involving in these spectra orbitals demonstrate that the catalysts are composed of Bi, O, F, I, and C. The characteristic binding energy value of 157.5-158.4 eV for Bi $4f_{7/2}$ **(Figure 3(a))** shows a trivalent oxidation state for bismuth. An additional spin–orbit doublet with binding the energy of 155.2-156.0 eV for Bi $4f_{7/2}$ is also revealed o all samples, suggesting that certain parts of bismuth exist in the (+3−x) valence state. This shows that the trivalent bismuth is partially reduced to the lower valence state through the hydrothermal method. A similar chemical shift of approximately 2.0 eV for Bi $4f_{7/2}$ was published by Liao *et al.* [2,5]. They found that the Bi $^{(+3-x)}$ formal oxidation state could most probably be ascribed to the sub-stoichiometric forms of Bi within the Bi_2O_2 layer, and the formation of the low oxidation state results in oxygen vacancies in the crystal lattice. However, this study assumes that the Bi $^{(+3-x)}$ formal oxidation state could most likely be ascribed to the sub-stoichiometric forms of Bi at the outer site of the particles, and the formation of the low oxidation state results in oxygen vacancies in the crystal surface, revealing that the main chemical states of the bismuth element in the samples are not trivalent. **Figure 3(b)** shows the high-resolution XPS spectra for the O 1s region of $Bi_{50}O_{59}F_{32}$/BiOI/GO composites, which could be resolved into two peaks; the main peak at 528.6 eV is attributed to the Bi–O bonds in the $(Bi_2O_2)^{2+}$ slabs of the BiOX layered structure, whereas the peak at 530.9 eV is assigned to the hydroxyl groups on the surface [25]. From **Figure 3(c)**, the binding energy of 686.2 eV is attributed to F 1s, respectively, which could be pointed to F at the monovalent oxidation state. From **Figure 3(d)**, the binding energy of 628.9 eV and 617.4 eV is attributed to I $3d_{5/2}$ and $3d_{3/2}$, respectively, which could be pointed to I at the monovalent oxidation state. **Figures 3(e)** shows the high-resolution C 1s spectrum of $Bi_{50}O_{59}F_{32}$/BiOI/GO composites and pure GO. Three carbon species are displayed mainly in the C 1s spectra of pure GO and $Bi_{50}O_{59}F_{32}$/BiOI/GO composites including un-oxidized carbons (sp^2 carbon), C−O, and C = O. As seen in **Figures 3(e)**, three different chemically shifted components are consisted, which could be de-convoluted into sp^2 carbons in aromatic rings (284.3 eV) and C atoms bonded to oxygen (C−O 286.7 eV) and carbonyl (C = O, 288.6 eV) [26]. The asymmetric O 1s peak shown in **Figure 3(b)** can be split by using the XPS peak-fitting program for pure GO. The peak at 529.9 eV is assigned to the external −OH group or the water molecule adsorbed on the surface, and the other O 1s peak appearing at 528.6 eV corresponds to the C-O bonds in the GO [2].

A series of BiO_mF_n/BiO_xI_y/GO composites are synthesized through hydrothermal methods at different pH values. The surface morphologies of the as-prepared samples are measured using FE-SEM-EDS. The FE-SEM image (**Figures 4**) displays that the morphologies of the samples acquired at different pH values turn from square-plate to flower-like, nanosheets, small-thin nanosheets, and then become irregular small-thin nanosheets. The SEM-EDS and TEM-EDS results demonstrate that the main elements within these samples are bismuth, oxygen, fluorine, iodine, and carbon. From the aforementioned results, a series of BiO_mF_n/BiO_xI_y/GO composites could be selectively synthesized through the controlled hydrothermal method.

As shown in **Figure 5** for the diffuse reflectance ultraviolet of various BiO_mF_n/BiO_xI_y/GO composites, the absorption edge of BiO_mF_n/BiO_xI_y is about 540 nm. The E_g value of BiO_pCl_q/BiO_xI_y/GO is determined from a plot of $(\alpha hv)^{1/2}$ vs. energy (hv), which is calculated as 1.92-2.30 eV. The results suggest that the fabrication of the BiO_mF_n/BiO_xI_y/GO composites could greatly improve the optical absorption property and increase the utilized efficiency of solar light, which is favorable for the enhancement of the photocatalytic activity.

The BET surface area of GO is measured to be 12.98 m^2g^{-1}; far below the theoretical value of fully exfoliated pristine graphene (∽2620 m^2g^{-1}). The pore volume and size of GO distribute to 0.016 cm^3g^{-1} and 5.32 nm. The isotherms of GO are close to Type III without a hysteresis loop at a high relative pressure between 0.6 and 1.0 [2], suggesting the existence of nonporous GO. The isotherms of BiO_xI_y and BiO_mF_n are close to Type IV with a hysteresis loop at a high relative pressure between 0.6 and 1.0 [2]. **Figure 6** shows the nitrogen adsorption–desorption isotherm curves of $Bi_{50}O_{59}F_{32}$/BiOI/GO. The BET surface area of the sample is measured to be 18.2 m^2g^{-1}. The pore

volume and size of the $Bi_{50}O_{59}F_{32}$/BiOI/GO composite sample are determined as the pore volume 0.269 cm^3/g and 8761 nm, respectively. The isotherms are close to Type IV with a hysteresis loop at a high relative pressure between 0.6 and 1.0. The shape of the hysteresis loop is close to H3, suggesting the existence of slit-like pores generally formed by the aggregation of plate-like particles, which is consistent with the self-assembled nanoplate-like morphology of samples. This result is consistent with the FE-SEM results, showing that self-assembled nanosheets result in the formation of hierarchical architectures.

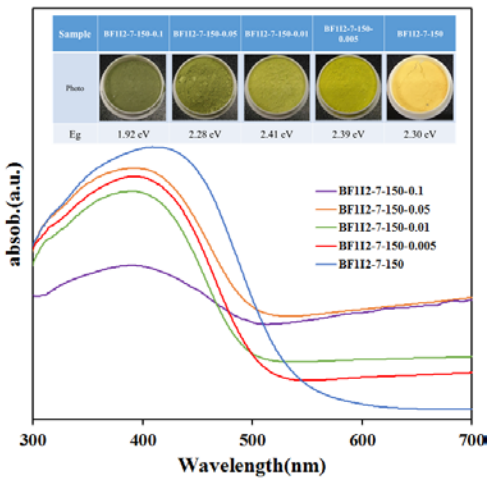

Figure 5. UV-vis absorption spectra of the as-prepared photocatalysts under different amount of GO (Hydrothermal conditions: molar ratio KF/KI = 1/2, GO = 0-0.1 g, Temp = 150 °C, pH = 7, Time = 12h).

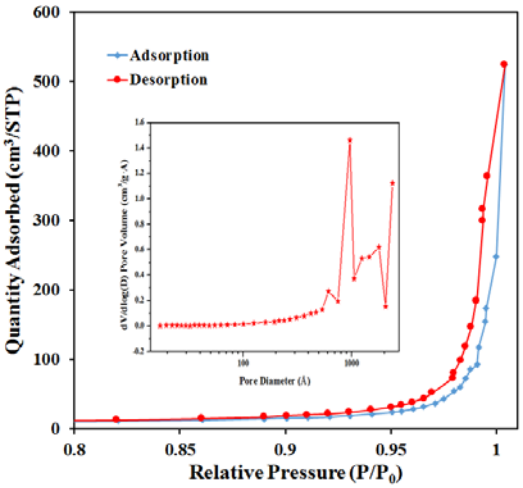

Figure 6. N_2 adsorption–desorption isotherm distribution curves and (inset) the pore distribution curves of $Bi_{50}O_{59}F_{32}$/BiOI/GO (BF1I2-7-150-0.05). (Hydrothermal conditions: Molar ratio KF/KI = 1/2, Temp = 150 °C, pH = 7, Time = 12h)

3.2 Photocatalytic activity

Figure 7 illustrates the changes in the ultraviolet visible (UV-vis) spectra during the photodegradation process of CV and SA in aqueous $Bi_{50}O_{59}F_{32}$/BiOI/GO dispersions under visible light irradiation. They are wholly degraded after visible light irradiation for 24 h, approximately 99% of CV and SA. During visible light irradiation, the characteristic absorption band of the CV dye at approximately 590.1 nm decreases rapidly with slight hypsochromic shifts (553.8 nm), but no new absorption band appears even in the ultraviolet range (λ > 200 nm), indicating the probable formation of a series of *N*-de-methylated intermediates and the cleavage of the whole conjugated chromophore structure of the CV dye. Further irradiation causes the decrease of absorption band at 553.8 nm, but no further wavelength shift is observed, inferring that the band at 553.8 nm is that of the full *N*-de-methylated product of the CV dye [2,6].

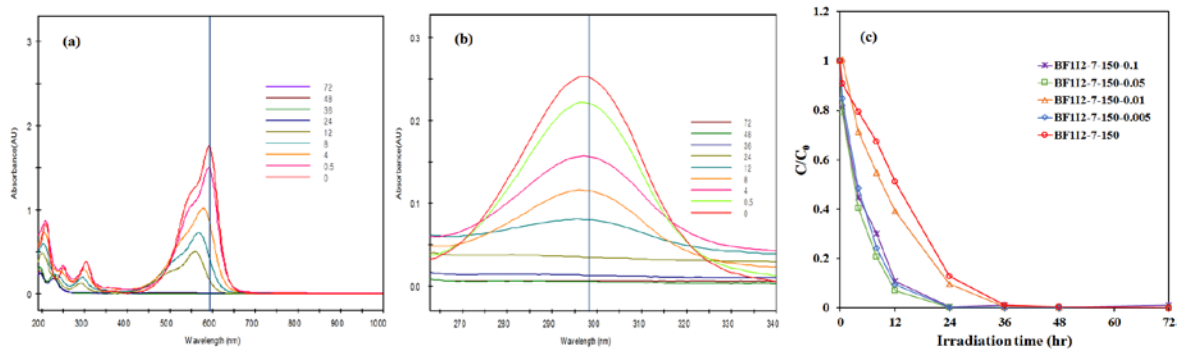

Figure 7. (a)(b) Temporal UV–vis adsorption spectral of CV and SA and (c) Photocatalytic degradation of CV as a function of irradiation time over different photocatalysts. (Hydrothermal condition: Molar ratio KF/KI= 1/2, GO = 0-0.1g, pH = 7, reaction temperature = 150ºC, reaction time 12h; 10mg/100mL photocatalyst, 10ppm CV)

Figure 7(c) illustrates the degradation efficiency as a function of reaction time; the removal efficiency is significantly enhanced in the presence of 0.005–0.1 g BiO_mF_n/BiO_xI_y/GO composites. To further understand the reaction kinetics of CV degradation, the apparent pseudo-first-order model [27], $ln(C_o/C) = kt$, is applied to the experiments. Through the first-order linear fit of the data shown in **Table 2**, the k values of $Bi_{50}O_{59}F_{32}$/BiOI/GO are obtained as the maximum degradation rates of 2.539×10^{-1} h^{-1} by using the first-order linear fit of the data, which are much higher than those of the other composites. **Table 2** shows a comparison among the rate constants of different photocatalysts. The order of rate constants appears $Bi_{50}O_{59}F_{32}$/BiOI/GO > BiOF/BiOI/GO > BiOI > $Bi_{50}O_{59}F_{32}$/BiOI/Bi_5O_7I/GO > BiOF > GO. The photocatalytic activity of $Bi_{50}O_{59}F_{32}$/BiOI/GO composites reaches a maximum rate constant of 0.2539 h^{-1}, which is 1.1 times higher than that of $Bi_{50}O_{59}F_{32}$/BiOI, 1.3 and 110 times higher than that of BiOI and $Bi_{50}O_{59}F_{32}$.

Sample	k (h^{-1})	R^2
BF1I2-1-150	0.0126	0.9189
BF1I2-1-150-0.005	0.0266	0.9307
BF1I2-1-150-0.01	0.0209	0.9828
BF1I2-1-150-0.05	**0.0338**	**0.9791**
BF1I2-1-150-0.1	0.028	0.9648
BF1I2-4-150	0.2305	0.9758
BF1I2-4-150-0.005	0.1848	0.9921
BF1I2-4-150-0.01	**0.2427**	**0.988**
BF1I2-4-150-0.05	0.1818	0.997
BF1I2-4-150-0.1	0.2217	0.9503
BF1I2-7-150	0.0824	0.9523
BF1I2-7-150-0.005	0.0967	0.9862
BF1I2-7-150-0.01	0.2365	0.9878
BF1I2-7-150-0.05	**0.2539**	**0.9889**
BF1I2-7-150-0.1	0.2158	0.9823
BF1I2-10-150	**0.1323**	**0.9549**
BF1I2-10-150-0.005	0.0424	0.972
BF1I2-10-150-0.01	0.0413	0.9804
BF1I2-10-150-0.05	0.117	0.9628
BF1I2-10-150-0.1	0.0155	0.9658
BF1I2-13-150	0.0005	0.0091
BF1I2-13-150-0.005	0.0533	0.9511
BF1I2-13-150-0.01	0.0477	0.9468
BF1I2-13-150-0.05	**0.0869**	**0.9877**
BF1I2-13-150-0.1	0.067	0.8624

Table 2. Pseudo-first-order rate constants for the degradation of CV with photocatalysts under visible light irradiation. (Hydrothermal conditions: molar ratio KF/KI = 1/2, GO = 0-0.1g, temp = 150°C, pH = 1-13, time = 12 h)

The durability of $Bi_{50}O_{59}F_{32}$/BiOI/GO composite is evaluated by recycling the used catalyst. After each cycle, the catalyst is collected by centrifugation. No apparent loss is observed in the photocatalytic activity when CV is removed in the 3rd cycle; even during the fifth run, the decline in photocatalytic activity appears 10% (**Figure 8(a)**). The used $Bi_{50}O_{59}F_{32}$/BiOI/GO composite is also examined by XRD and no detectable difference is observed between the as-prepared and the used samples (**Figure 8(b)**); hence, the $Bi_{50}O_{59}F_{32}$/BiOI/GO composite has excellent photostability.

Presumably, the enhanced photocatalytic activities of BiO_mF_n/BiO_xI_y/GO composites could be

ascribed to a synergistic effect including a high BET surface area, the formation of the composites (or heterojunction), a layered structure, and the low energy band structure. In the absence of photocatalysts, CV could not be degraded under visible light irradiation; the superior photocatalytic ability of BiO_mF_n/BiO_xI_y/GO may be ascribed to its efficient utilization of visible light and high separation efficiency of the electron–hole pairs within its composites.

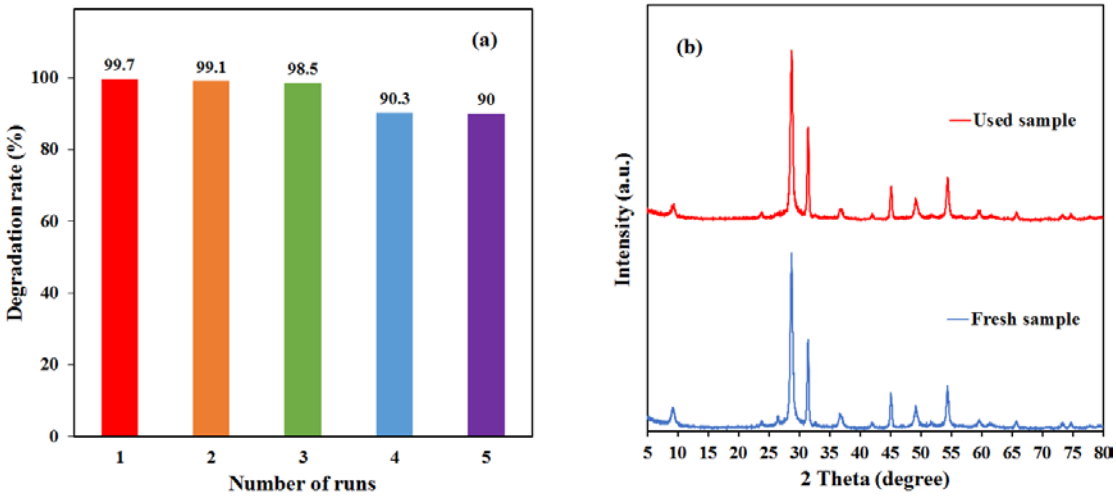

Figure 8. (a) Cycling runs and (b) XRD patterns acquired before and after in the photocatalytic degradation of CV in the presence of $Bi_{50}O_{59}F_{32}$/BiOI/GO.

3.3 Active Species

In general, three proposed possible reaction mechanisms are involved in the photodegradation of organisms by a semiconductor, including (i) photocatalysis, (ii) photolysis, and (iii) dye photosensitization [28]. Various primary active species, such as hydroxyl radical, hole, superoxide radical**,** hydrogen radical ($H^{\bullet}$**),** and singlet oxygen, could be generated during photo-catalytic decomposition processes in UV-vis/semiconductor systems. Dimitrijevic *et al.* [29] proposed that water, which dissociated both on the surface of TiO_2 and in subsequent molecular layers, had a three-fold role as (i) a stabilizer of charges, preventing electron–hole recombination; (ii) as an electron acceptor, forming H atoms in a reaction of photogenerated electrons with protons on the surface, $–OH_2^+$; and (iii) an electron donor, resulting in the reaction of water with photogenerated holes to give $^{\bullet}$OH radicals.

When GO is combined with other materials, electrons would flow from one material to another (from a higher to a lower Fermi level) to align the Fermi energy levels at the interface of two materials [30]. Bai *et al.* [31] reported that active species trapping measurements, superoxide radicals ($O_2^{-\bullet}$) and hydroxy radicals ($^{\bullet}$OH) played a crucial role during the catalytic process in the methylene blue degradation process using $ZnWO_4$/graphene hybrids. Wang *et al.* [32] revealed that $O_2^{-\bullet}$ and $^{\bullet}$OH were the main reactive species for the degradation of rhodamine B with $BiVO_4$/rGO. The hydroxyl radical $HO^{\bullet}$ might only be formatted through an $e^- \rightarrow O_2^{-\bullet} \rightarrow H_2O_2 \rightarrow {}^{\bullet}OH$ route. However, $^{\bullet}$OH radical was formatted through the multistep reduction of $O_2^{-\bullet}$ in the system [33]. According to a previous study [31], a photocatalytic process was governed mainly by $O_2^{-\bullet}$ rather than by $^{\bullet}$OH, e^-, or h^+. In a previous study [5], the CV photodegradation by BiO_mX_n/BiO_pY_q (X, Y = Cl, Br, I) under visible light was dominated by oxidation with $O_2^{-\bullet}$ being the main active species and $^{\bullet}$OH and h^+ being the minor active species. On the basis of the aforementioned references, the probability of forming $^{\bullet}$OH should be much lower than that for $O_2^{-\bullet}$; however, $^{\bullet}$OH is an extremely strong and nonselective oxidant, which leads to a partial or complete mineralization of several organic chemicals.

To revaluate the effect of the active species during the photocatalytic reaction, a series of quenchers are introduced to scavenge the relevant active species. As shown in **Figure 9**, the photocatalytic degradation of CV is not affected by the addition of AO, whereas the degradation efficiency of BQ, IPA, and SA quenching evidently decrease when compared with that of no quenching. $O_2^{\bullet-}$ is a major

active species and ·OH and $^1O_2$ are minor active species in the process of photocatalytic degradation of CV. Therefore, the quenching effects of different scavengers and EPR indicate that reactive $O_2^{\bullet-}$ plays a major role and ·OH and $^1O_2$ play a minor role in CV photocatalytic degradation.

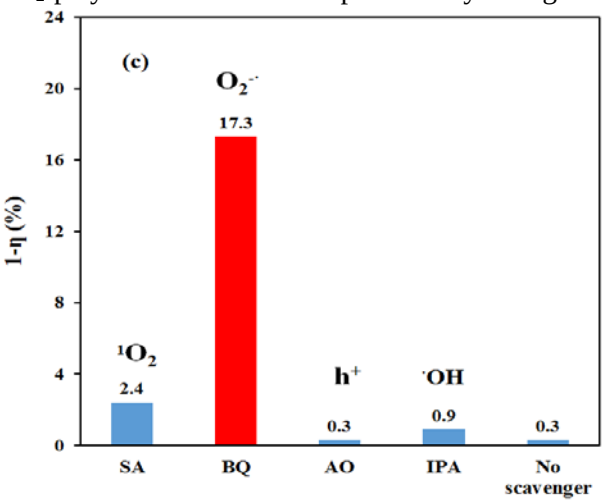

Figure 9. The CV concentration during photodegradation as a function of irradiation time observed in $Bi_{50}O_{59}F_{32}$/BiOI/GO under the addition of different scavengers: SA, IPA, AQ, and BQ.

On the basis of the aforementioned experimental results, a detailed pathway of decomposition is illustrated in **Figure 10.** Once the electron reaches the conduction band of BiO_xX_y (X = Cl, I), it induces the formation of active oxygen species, which causes the decomposition of CV dye. Both photo-sensitized and photo-catalytic processes are proceeded concurrently (**Figure 10**). However, in photo-sensitized and photo-catalytic reaction conditions, $O_2^{\bullet-}$ radicals are formatted by the reaction of photogenerated and photosensitized electron with oxygen gas on the photocatalyst surface; hydroxyl radicals are also produced by the reaction of $O_2^{\bullet-}$ radicals with H^+ ion and hole h^+ with OH^- ion (or H_2O). The hydroxyl radicals are produced subsequently [34]. This cycle continuously occurs when the system is exposed to visible light irradiation [3]. To understand this unexpected result, the mechanism of $^1O_2$ formation is more closely examined during photoexcitation of BiO_mF_n/BiO_xI_y/GO photocatalyst. $^1O_2$ also can be produced via the electron transfer between superoxide $O_2^{\bullet-}$ and cation species with appropriate oxidizing power [35]. Photogenerated h^+ in semiconductor nanoparticles could be such cation species to oxidize $O_2^{\bullet-}$. This mechanism for the production of $^1O_2$ during photoexcitation of ZnO has been reported [36]; after several cycles of photooxidation, the decomposition of CV by the generated oxidant species can be expressed by Eqs. 1–3.

$$CV + O_2^{-\bullet} \rightarrow \text{decomposed compounds} \quad (1)$$
$$CV + OH^{\bullet} \rightarrow \text{decomposed compounds} \quad (2)$$
$$CV + {}^1O_2 \rightarrow \text{decomposed compounds} \quad (3)$$

Hydroxylated compounds are identified for the photocatalytic degradation of CV under visible light-induced semiconductor systems [5]. Under UV light irradiation, *N*-dealkylation processes are preceded by the formation of a nitrogen-centered radical, and the destruction of the dye chromophore structure is preceded by the generation of a carbon-centered radical in the photocatalytic degradation of the CV dye [2, 3, 34]. All the intermediates identified in these two researched topics have the same results under UV or visible light irradiation. Although the photocatalytic and photosensitized processes proceed concurrently, $O_2^{\bullet-}$ is formed by the reaction of photogenerated and photosensitized e^- with O_2 on the photocatalyst surface, whereas ·OH is formed by the reaction of $O_2^{\bullet-}$ with H^+ and h^+ with OH^- (or H_2O). Notably, the hydroxyl radical $HO^{\bullet}$ might only be generated through the $e^- \rightarrow O_2^{-\bullet} \rightarrow H_2O_2 \rightarrow {}^{\bullet}OH$ route, whereas the ·OH radical is generated through a multistep $O_2^{-\bullet}$ reduction. Undoubtedly, the major oxidant is ·OH radicals, not $O_2^{-\bullet}$ radicals. The reaction pathways of BiO_mF_n/BiO_xI_y/GO-mediated photocatalytic processes proposed in this study should offer some guidance for applications in the decomposition of dyes.

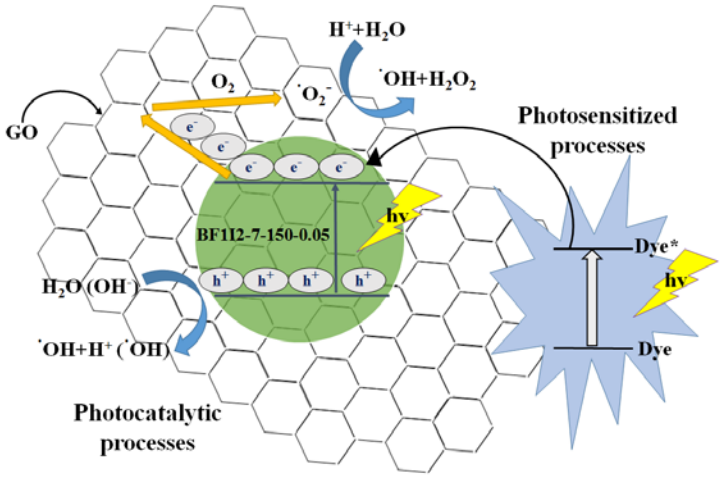

Figure 10. Schematic illustration of the band gap structures of $Bi_{50}O_{59}F_{32}$/BiOI/GO

4 CONCLUSIONS

This is the first report where $Bi_{50}O_{59}F_{32}$/BiOI/GO -assisted photocatalytic degradation of the CV dye under visible light irradiation is synthesized through a simple hydrothermal method. The assembled $Bi_{50}O_{59}F_{32}$/BiOI/GO exhibits excellent photocatalytic activity in the degradation of CV under visible light irradiation. The order of rate constants appears $Bi_{50}O_{59}F_{32}$/BiOI/GO > BiOF/BiOI/GO > BiOI > $Bi_{50}O_{59}F_{32}$/BiOI/Bi_5O_7I/GO > BiOF > GO. The photocatalytic activity of $Bi_{50}O_{59}F_{32}$/BiOI/GO composites reaches a maximum rate constant of 0.2539 h^{-1}, which is 1.1 times higher than that of $Bi_{50}O_{59}F_{32}$/BiOI, 1.3 and 110 times higher than that of BiOI and $Bi_{50}O_{59}F_{32}$.Thus, the $Bi_{50}O_{59}F_{32}$/BiOI/GO composites play a major role in enhancing photocatalytic activity. The quenching effects of different scavengers demonstrated that reactive $O_2^{\bullet-}$ plays a major role in CV degradation. Chiefly, composite systems exhibit adequate catalytic activity and stability, acting as authentic heterogeneous visible-light-driven photocatalysts in degrading organic pollutants efficiently.

ACKNOWLEDGEMENTS

This research was supported by the Ministry of Science and Technology of Taiwan (MOST-105-2113-M-142-001).

REFERENCES

[1] Kubacka, M. Fernández-García, and G. Colón, Advanced Nanoarchitectures for Solar Photocatalytic Applications, *Chem. Rev*. **112**, 2012, pp.1555-1614. (doi: 10.1021/cr100454n)

[2] Y.R. Jiang, H.P. Lin, W.H. Chung, Y.M. Dai, W.Y. Lin, C.C. Chen, Controlled hydrothermal synthesis of BiO_xCl_y/BiO_mI_n composites exhibiting visible-light photocatalytic degradation of crystal violet, *J. Hazard. Mat*. **283**, 2015, pp. 787-805.(doi: 10.1016/j.jhazmat.2014.10.025)

[3] Y. R. Jiang, S. Y. Chou, J. Lin Chang, S. T. Huang, H. P. Lin, C. C. Chen, Hydrothermal Synthesis of Bismuth Oxybromide-Bismuth Oxyiodide Composites with highly visible light Photocatalyticperformance for the degradation of CV and Phenol, *RSC Adv*. **5**, 2015, pp. 30851-30860. (doi:10.1039/C5RA01702E)

[4] W.L.W. Lee, W.H. Chung, W.S. Huang, W.C. Lin, W.Y. Lin, Y.R. Jiang and C.C. Chen, Photocatalytic activity and mechanism of nano-cubic barium titanate prepared by a hydrothermal method, *J. Taiwan Inst. Chem. Eng.* **44**, 2013, pp. 660-669. (doi:10.1016/j.jtice.2013.01.005)

[5] W. W. Lee, C. S. Lu, C. W. Chuang, Y. J. Chen, J. Y. Fu, C. W. Siao and C. C. Chen, Synthesis of bismuth oxyiodides and their composites: characterization, photocatalytic activity, and degradation mechanisms, *RSC Adv*. **5**, 2015, pp. 23450-23463. (doi:10.1039/C4RA15072D)

[6] W.L.W. Lee, J.S. Lin, J.L. Chang, J.Y. Chen, M.C. Cheng and C.C. Chen, Photodegradation of CV over nanocrystalline bismuth tungstate prepared by hydrothermal synthesis, *J. Mol. Catal. A: Chem.* **361–362**, 2012, pp. 80-90.(doi:10.1016/j.molcata.2012.04.015)

[7] K. Yu, S. Yang, C. Liu, H. Chen, H. Li, C. Sun and S.A. Boyd, Degradation of Organic Dyes via Bismuth Silver Oxide Initiated Direct Oxidation Coupled with Sodium Bismuthate Based Visible Light Photocatalysis, *Environ. Sci. Technol.* **46**, 2012, pp.7318-7326. (doi:10.1021/es3001954)

[8] S. Y. Chou, W. H. Chung, L. W. Chen, Y. M. Dai, W. Y. Lin, J. H. Lin and C. C. Chen, A series of BiOxIy/GO photocatalysts: synthesis, characterization, activity, and mechanism, *RSC Adv.* **6**, 2016, pp. 82743-82758. (doi:10.1039/C6RA12482H)

[9] C. T. Yang , W. W. Lee, H. P. Lin, Y. M. Dai, H. T. Chi, C. C. Chen, A novel heterojunction Bi_2SiO_5/g-C_3N_4: Synthesis, characterization, photocatalytic activity, and mechanism, *RSC Adv.* **6**, 2016, pp. 40664-40675. (doi:10.1039/C6RA02299E)

[10] H. P. Lin, C. C. Chen, W. W. Lee, Y. Y. Lai, J. Y. Chen, Y. Q. Chen and J. Y. Fu, Synthesis of $SrFeO_{3-x}$/g-C_3N_4 heterojunction with improved visible-light photocatalytic activities in chloramphenicol and crystal violet degradation, *RSC Adv.* **6**, 2016, pp. 2323-2336. (doi:10.1039/C5RA21339H)

[11] Jie Li, Ying Yu and Lizhi Zhang, Bismuth oxyhalide nanomaterials: layered structures meet photocatalysis, *Nanoscale*, **6**, 2014, pp. 8473-8488. (doi:10.1039/C4NR02553A)

[12] X. Xiao, C. Xing, G. He, X. Zuo, J. Nan and L. Wang, Solvothermal synthesis of novel hierarchical $Bi_4O_5I_2$ nanoflakes with highly visible light photocatalytic performance for the degradation of 4-tert-butylphenol, *Appl. Catal. B: Environ.* **148-149**, 2014, pp. 154-163. (doi:10.1016/j.apcatb.2013.10.055)

[13] W.L. Huang and Q.S. Zhu, DFT calculations on the electronic structures of BiOX (X = F, Cl, Br, I) photocatalysts with and without semicore Bi 5d states, *J. Comput. Chem.* **30**, 2009, pp. 183-190. (doi: 10.1002/jcc.21055)

[14] X. Xiao, C. Liu, R. Hu, X. Zuo, J. Nan, L. Li and L. Wang, Oxygen-rich bismuth oxyhalides: generalized one-pot synthesis, band structures and visible-light photocatalytic properties, *J. Mater. Chem.* **22**, 2012, pp. 22840-22843. (doi:10.1039/C2JM33556E)

[15] E. Keller, V. Kramer, A strong deviation from Vegard's rule: x-ray powder investigations of the three quasi-binary phase systems BiOX-BiOY (X,Y = Cl, Br, I), *Z. Naturforsch.* **60b**, 2005, pp. 1255-1263. (doi:200902292949663526)

[16] Q. Xiang, J. Yu and M. Jaroniec, Graphene-based semiconductor photocatalysts, *Chem. Soc. Rev.* **41**, 2012, pp. 782-796. (doi:10.1039/C1CS15172J)

[17] H. Liu, W. R. Cao, Y. Su, Z. Chen, Y. Wang, Bismuth Oxyiodide–Graphene Nanocomposites with High Visible Light Photocatalytic Activity, *J. Colloid Interface Sci.* **398**, 2013, pp. 161-167. (doi:10.1016/j.jcis.2013.02.007)

[18] X. X. Wei, C. M. Chen, S. Q. Guo, F. Guo, X. M. Li, X. X. Wang, H. T. Cui, L. F. Zhao, W. Li, Advanced Visible-Light-Driven Photocatalyst BiOBr–TiO_2–Graphene Composite with Graphene as a Nano-Filler, *J. Mater. Chem. A.* 2, **2014**, pp. 4667-4675. (doi:10.1039/C3TA14349J)

[19] I. V. Lightcap, T. H. Kosel, P. V. Kamat, Anchoring Semiconductor and Metal Nanoparticles on a Two-Dimensional Catalyst Mat. Storing and Shuttling Electrons with Reduced Graphene Oxide, *Nano Lett.* **10**, 2010, pp. 577-583.(doi: 10.1021/nl9035109)

[20] S. Song, B. Cheng, N. Wu, A. Meng, S. Cao, J. Yu, Structure Effect of Graphene on the Photocatalytic Performance of Plasmonic Ag/Ag_2CO_3-rGO for Photocatalytic Elimination of Pollutants, *Appl. Catal. B: Environ.* 181, 2016, pp. 71-78. (doi:10.1016/j.apcatb.2015.07.034)

[21] A. Bhirud, S. Sathaye, R. Waichal, C. J. Park, B. Kale, In Situ Preparation of N–ZnO/graphene Nanocomposites: Excellent Candidate as a Photocatalyst for Enhanced Solar Hydrogen Generation and High Performance Supercapacitor Electrode, *J. Mater. Chem. A.* **3**, 2015, pp. 17050-17063. (doi:10.1039/C5TA03955J)

[22] W. S. Hummers and R. E. Offeman, Preparation of Graphitic Oxides, *J. Am. Chem. Soc.* **80**, 1958, pp. 1339. (doi/pdf/10.1021/ja01539a017)

[23] X. Xiao and W.D. Zhang, Hierarchical $Bi_7O_9I_3$ micro/nano-architecture: facile synthesis, growth mechanism, and high visible light photocatalytic performance, *RSC Adv.* **1**, 2011, pp. 1099-1105. (doi:10.1039/C1RA00323B)

[24] H. Liu, Y. Su, Z. Chen, Z. Jin, Y. Wang, $Bi_7O_9I_3$/Reduced Graphene Oxide Composite as an Efficient Visible-Light-Driven Photocatalyst for Degradation of Organic Contaminants, *J. Mol. Catal. A: Chem.* **391**, 2014, pp. 175-182. (doi:10.1016/j.molcata.2014.04.029)

[25] F. Dong, Y. Sun, M. Fu, Z. Wu, S. C. Lee, Room Temperature Synthesis and Highly Enhanced Visible Light Photocatalytic Activity of Porous BiOI/BiOCl Composites Nanoplates Microflowers, *J. Hazard. Mater.* **219-220**, 2012, pp. 26-34. (doi: 10.1016/j.jhazmat.2012.03.015)

[26] D. Chen, H. Feng, J. Li, Graphene Oxide: Preparation, Functionalization, and Electrochemical Applications, *Chem. Rev.* **112**, 2012, pp. 6027-6053. (doi/pdf/10.1021/cr300115g)

[27] A. Chatzitakis, C. Berberidou, I. Paspaltsis, G. Kyriakou, T. Sklaviadis, and I. Poulios, Photocatalytic degradation and drug activity reduction of Chloramphenicol, *Water Res.* **42**, 2008, pp. 386-394. (doi:10.1016/j.watres.2007.07.030)

[28] C. Nasr, K. Vinodgopal, L. Fisher, S. Hotchandani, A. K. Chattopadhyay and P. V. Kamat, Environmental Photochemistry on Semiconductor Surfaces. Visible Light Induced Degradation of a Textile Diazo Dye, Naphthol Blue Black, on TiO_2 Nanoparticles, *J. Phys. Chem.* **100**, 1996, pp. 8436-8442. (doi/pdf/10.1021/jp953556v)

[29] N.M. Dimitrijevic, B.K. Vijayan, O.G. Poluektov, T. Rajh, K.A. Gray, H. He and P. Zapol, Role of Water and Carbonates in Photocatalytic Transformation of CO_2 to CH_4 on Titania, *J. Am. Chem. Soc.* **133**, 2011, pp. 3964-3971. (doi:10.1021/ja108791u)

[30] H. Y. Mao, S. Laurent, W. Chen, O. Akhavan, M. Imani, A. A. Ashkarran, M. Mahmoudi, Graphene: Promises, Facts, Opportunities, and Challenges in Nanomedicine, *Chem. Rev.* **113**, 2013, pp. 3407-3424.(doi/pdf/10.1021/cr300335p)

[31] X. Bai, L. Wang, Y. Zhu, Visible Photocatalytic Activity Enhancement of $ZnWO_4$ by Graphene Hybridization, *ACS Catal.* **2**, 2012, pp. 2769-2778. (doi:10.1021/cs3005852)

[32] Y. Wang, W. Wang, H. Mao, Y. Lu, J. Lu, J. Huang, Z. Ye, B. Lu, Electrostatic Self-Assembly of $BiVO_4$–Reduced Graphene Oxide Nanocomposites for Highly Efficient Visible Light Photocatalytic Activities, *ACS Appl. Mater. Interfaces*, **6**, 2014, pp. 12698-12706. (doi/pdf/10.1021/am502700p)

[33] S.T. Huang, Y.R. Jiang, S.Y. Chou, Y.M. Dai and C.C. Chen, Synthesis, characterization, photocatalytic activity of visible-light-responsive photocatalysts BiO_xCl_y/BiO_mBr_n by controlled hydrothermal method, *J. Mol. Catal. A: Chem.* **391**, 2014, pp. 105-120. (doi:10.1016/j.molcata.2014.04.020)

[34] H. J. Fan, C. S. Lu, W. L. W. Lee, M. R. Chiou and C. C. Chen, Mechanistic pathways differences between P25-TiO2 and Pt-TiO2 mediated CV photodegradation, *J. Hazard. Mater.* **185**, 2011, pp. 227-235. (doi: 10.1016/j.jhazmat.2010.09.022)

[35] W. He, H. Jia, W. G. Wamer, Z. Zheng, P. Li, J. H. Callahan, J. J. Yin, Predicting and identifying reactive oxygen species and electrons for photocatalytic metal sulfide micro–nano structures, *J. Catal.* **320**, 2014, pp. 97-105. (doi:10.1016/j.jcat.2014.10.004)

[36] W. He, H. K. Kim, W. G. Wamer, D. Melka, J. H. Callahan, and J. J. Yin, Photogenerated Charge Carriers and Reactive Oxygen Species in ZnO/Au Hybrid Nanostructures with Enhanced Photocatalytic and Antibacterial Activity, *J. Am. Chem. Soc.* **136**, 2014, pp. 750-757. (doi/pdf/10.1021/ja410800y)